

An electron-spin qubit platform assembled atom-by-atom on a surface

Yu Wang^{1,2,†}, Yi Chen^{1,2,†}, Hong T. Bui^{1,3,†}, Christoph Wolf^{1,2}, Masahiro Haze^{1,4}, Cristina Mier^{1,5}, Jinkyung Kim^{1,3}, Deung-jang Choi^{1,5,6,7}, Christopher P. Lutz⁸, Yujeong Bae^{1,3,*}, Soohyon Phark^{1,2,*}, Andreas J. Heinrich^{1,3,*}

¹Center for Quantum Nanoscience, Institute for Basic Science (IBS), Seoul 03760, Korea

²Ewha Womans University, Seoul 03760, Korea

³Department of Physics, Ewha Womans University, Seoul 03760, Korea

⁴The Institute for Solid State Physics, University of Tokyo, Kashiwa 277-8581, Japan

⁵Centro de Física de Materiales CFM/MPC (CSIC-UPV/EHU), 20018 Donostia-San Sebastián, Spain

⁶Donostia International Physics Center (DIPC), 20018 Donostia-San Sebastián, Spain

⁷Ikerbasque, Basque Foundation for Science, 48013 Bilbao, Spain

⁸IBM Research Division, Almaden Research Center, San Jose, CA 95120, USA

*Corresponding authors. Email: bae.yujeong@qns.science, phark@qns.science, heinrich.andreas@qns.science

†These authors contributed equally to this work.

Creating a quantum-coherent architecture at the atomic scale has long been an ambition in quantum science and nanotechnology^{1,2}. This ultimate length scale requires the use of fundamental quantum properties of atoms, such as the spin of electrons, which naturally occurs in many solid-state environments and allows high-fidelity operations and readout by electromagnetic means³⁻⁵. Despite decades of effort, however, it remains a formidable task to realize an atomic-scale quantum architecture where multiple electron spin qubits can be

precisely assembled, controllably coupled, and coherently operated. Electron spin qubits created in dopants in semiconductors and color centers in insulators, for example, can be well controlled individually⁶⁻⁸ but are difficult to couple together into a circuit. On the other hand, multiple magnetic atoms and molecules on surfaces can be coupled to each other by building sophisticated atomic structures using a scanning tunneling microscope (STM)⁹⁻¹³, but coherent operation has so far been limited to a single qubit in the tunnel junction^{14,15}. Here we demonstrate an atomic-scale qubit platform by showing atom-by-atom construction, coherent operations, and readout of multiple electron-spin qubits on a surface. To enable the coherent control of “remote” qubits that are outside the tunnel junction, we complement each electron spin with a local magnetic field gradient from a nearby single-atom magnet^{16,17}. To enable readout of remote qubits, we employ a sensor qubit in the tunnel junction and implement pulsed double electron spin resonance. Using these methods, we demonstrate fast single-, two-, and three-qubit operations in an all-electrical fashion. Our work marks the creation of an Angstrom-scale qubit platform, where quantum functionalities using electron spin arrays, built atom-by-atom on a surface, are now within reach.

Constructing and coherently controlling novel nanoscale qubit systems lie at the heart of quantum-coherent nanoscience¹⁸⁻²⁰. An attractive approach is to employ atomic-level fabrication by a scanning tunneling microscope (STM), whereby atom manipulation^{9,21,22} or selective desorption^{6,23} can lead to designed quantum spin architectures. As a first step towards *in situ* operation of atomic quantum devices, a radio-frequency (RF) voltage has been used to coherently control a single electron spin in the STM tunnel junction^{14,15}, whose spin states can be read out through spin-polarized tunnel current^{10,12,24-27} in a so-called ESR-STM setup (ESR: electron spin

resonance)²⁸. However, harnessing the quantum functionalities of this platform requires multiple addressable qubits that lie outside the sub-nanometer tunnel junction region.

Figure 1a illustrates our strategy to construct such an atomic-scale multi-qubit platform. Addressable “remote” qubits are created on a bilayer MgO film by positioning a spin-1/2 hydrogenated Ti atom^{11,29} ~0.6 nm away from a single-atom magnet (Fe)³⁰ using STM-based atom manipulation (see Methods). Fe atoms are used here to supply a local magnetic field gradient, which can convert a tip-induced radio-frequency (RF) electric field into an effective driving magnetic field^{31,32}, in analogy to micromagnet driving in quantum dots³³. These qubits remain remote from the STM tunnel junction to avoid decoherence induced by the tunnel current. To enable readout, a sensor qubit consisting of a Ti atom is positioned in the tunnel junction and is weakly coupled to the remote qubits. Initialization is performed thermally by cooling the sample to 0.4 K and applying an external magnetic field, producing a thermal spin state having a predominant population in the spin ground state (~90% under a 0.7 T field).

A representative structure composed of two remote qubits and one sensor qubit is constructed atom-by-atom using atom manipulation (see Methods), as shown in Fig. 1b,c. The qubit-qubit couplings are sensitive to their atomic separations down to the Angstrom level^{11,12,29} (Extended Data Figs. 1 and 2), consistent with results in other material systems³⁴. This atomically-precise construction scheme thus allows us to engineer the resonant frequencies and couplings among all the spins, an essential step for addressing and detecting the multiple qubits individually (see Methods).

Detection of the remote qubits is achieved through ESR spectroscopy of the sensor qubit, whose ESR transition frequency depends on the quantum states of other qubits (Fig. 1d,e). The ESR frequencies of the qubits are designed to be sufficiently separated (see Methods and Extended

Data Fig. 1) that the multi-qubit states are well described by Zeeman product states, where we use blue (red) brackets to denote the quantum states of the sensor (remote) qubit. In a structure composed of a sensor qubit and a remote qubit (Fig. 1d), the two ESR transitions of the sensor qubit at frequencies f_1 (corresponding to transition $|0\rangle|0\rangle \leftrightarrow |1\rangle|0\rangle$) and f_2 ($|0\rangle|1\rangle \leftrightarrow |1\rangle|1\rangle$) detect the populations of $|0\rangle$ and $|1\rangle$ states of the remote qubit, respectively. Multiple remote qubits can be simultaneously sensed in a similar fashion (Fig. 1e).

To demonstrate this qubit control and readout scheme, we begin by measuring a remote qubit's ESR spectrum with the tip positioned above the sensor qubit, as sketched in Fig. 2a. The energy levels and ESR transitions of this two-qubit structure are illustrated in Fig. 2b and its STM image is shown in Fig. 1b. In order to individually address the sensor and remote qubits, we use two RF sources to apply two consecutive RF voltage pulses to the STM tip. A control pulse is applied at frequency f_R to control the remote qubit, followed by a sensing pulse at frequency f_S acting on the sensor qubit (Fig. 2b,c). A sensing pulse applied at $f_S = f_1$ (f_2) results in an ESR signal that depends on the population of state $|0\rangle$ ($|1\rangle$) of the remote qubit. To obtain the ESR spectrum of the remote qubit, we sweep the frequency f_R of the control pulse across the remote qubit resonances while keeping the sensing pulse fixed at a resonance frequency of the sensor qubit. When f_R matches an ESR transition of the remote qubit (e.g., $|0\rangle|0\rangle \leftrightarrow |0\rangle|1\rangle$), the joint two-qubit state populations are altered, resulting in a detectable decrease (increase) of the sensor's ESR signal at f_1 (f_2) (Fig. 2d and Methods). This measurement is conceptually similar to ensemble double electron spin resonance spectroscopy³⁵ and allows us to directly obtain the resonance frequencies of the remote qubit (f_3 and f_4 , see Fig. 2d) even though no tunnel current passes through it.

Single-qubit control is performed in our platform by coherently driving a qubit independent of other qubits' quantum states. This is achieved by exciting all ESR transitions of a remote qubit with the same driving strength¹⁴, as illustrated in the insets of Fig. 2e,f. The coherent rotation of a remote qubit on its Bloch sphere can be conducted by varying the pulse duration τ_R of the control pulse. A subsequent sensing pulse at f_1 reveals coherent Rabi oscillations of the remote qubit (Fig. 2e).

Two-axis control³⁶ of the remote qubit is demonstrated by varying the relative phase ϕ of two $\pi/2$ -pulses (Fig. 2f). On the Bloch sphere in the rotating frame, the first $\pi/2$ -pulse rotates the qubit from the z -axis to the y -axis, and the second performs a $\pi/2$ -rotation around an axis in the x - y plane at an angle of ϕ to the x -axis (lower inset, Fig. 2f). The resulting signal is well described by the expected $\cos(\phi)$ dependence (Fig. 2f)³⁶. Two-axis control allows arbitrary single-qubit operations as discussed in Ref.³⁷.

We next discuss two-qubit operations. Controlled NOT (CNOT) operations are straightforward to carry out in our platform by selectively exciting ESR transitions that correspond to a specific quantum state of a control qubit. In the case of a two-qubit structure, a CNOT operation of the remote qubit can be performed by driving a single ESR transition such as $|0\rangle|0\rangle \leftrightarrow |0\rangle|1\rangle$ at $f_R = f_3$ (Fig. 3a), which inverts the remote qubit only if the sensor qubit is in state $|0\rangle$. The quantum state of the remote qubit is then measured by applying a sensing pulse at f_1 (Fig. 3a). Sensing at f_2 (instead of at f_1) shows oscillations of the opposite sign because this effectively detects the population of state $|1\rangle$ (instead of state $|0\rangle$) of the remote qubit (Extended Data Fig. 4)³⁸. The oscillations in Fig. 3a show a CNOT operation time of ~ 13 ns for the remote qubit. The operation rate increases in proportion to the RF amplitude (Fig. 3b upper, Extended Data Fig. 3a). This fast operation results from the strong magnetic field gradient of the neighboring Fe atom. In contrast,

ESR of the sensor qubit, as well as previous ESR-STM spectroscopy^{11,27,32}, relies on the tip's magnetic field gradient. A consequence of driving by the surface Fe is that the CNOT rate is independent of time-average tunnel current I_{DC} , which corresponds to the tip's proximity (Fig. 3b lower, Extended Data Fig. 3b).

To evaluate the effect of the CNOT operation on the remote qubit, we perform controlled rotations of the sensor qubit without and with this CNOT operation (Fig. 3c,d). Since the initial thermal population of the two-qubit system is predominantly in state $|0\rangle|0\rangle$, a controlled rotation of the sensor qubit at f_1 starting from the initial state $|0\rangle|0\rangle$ (i.e., without a CNOT operation) shows clear oscillations because a pulse at f_1 excites the transition $|0\rangle|0\rangle \leftrightarrow |1\rangle|0\rangle$. Whereas measurement at transition f_2 shows no obvious oscillations¹⁴ (Fig. 3c) because remote qubit state $|1\rangle$ is nearly unoccupied. These coherent oscillations are reversed after a CNOT operation of the remote qubit at f_3 (Fig. 3d), which transfers the predominant population from state $|0\rangle|0\rangle$ to state $|0\rangle|1\rangle$, hence becoming accessible to a sensing pulse at $f_s = f_2$ (i.e., $|0\rangle|1\rangle \leftrightarrow |1\rangle|1\rangle$) but not f_1 ³⁹. We further verify that a CNOT operation of the remote qubit at f_4 (instead of f_3) does not significantly affect the oscillations observed on the sensor qubit (Extended Data Fig. 6), highlighting the selective, controlled nature of CNOT operations.

Although single- and two-qubit operations are sufficient to generate arbitrary quantum circuits⁴⁰, multi-qubit operations can significantly reduce the execution time and mitigate accumulated operation errors^{41,42}. As long as the qubit-qubit couplings can be spectroscopically resolved, our platform allows fast, native qubit operations having multiple control qubits (by selectively exciting certain ESR transitions). To demonstrate this ability, we construct a three-qubit structure composed of two remote qubits (referred to as RQ1 and RQ2) and a sensor qubit

(as sketched in Fig. 4a and imaged in Fig. 1c). We selectively drive RQ1's $|0\rangle|00\rangle \leftrightarrow |0\rangle|10\rangle$ transition (Extended Data Fig. 7a), corresponding to a rotation of RQ1 if and only if the sensor qubit and RQ2 are both in state $|0\rangle$ (Fig. 4a). When varying the pulse duration τ_R , this controlled-controlled operation is seen to cause oscillating populations between states $|00\rangle$ and $|10\rangle$ of the two remote qubits, whereas populations of states $|01\rangle$ and $|11\rangle$ are left unchanged (Fig. 4b). Here the changes of populations are determined from the intensities of the four ESR transitions of the sensor qubit (blue pulse in Fig. 4a). Similarly, the controlled-controlled operation $|0\rangle|01\rangle \leftrightarrow |0\rangle|11\rangle$ is seen to cause oscillating populations between states $|01\rangle$ and $|11\rangle$ of the two remote qubits, albeit with reduced amplitudes due to reduced initial thermal populations in these states (Extended Data Fig. 7e). From these measurements we obtain a controlled-controlled NOT (CCNOT) operation time as short as 20 ns. Single-, two-, and multi-qubit gates in our platform have comparably fast operation times because they only differ in the frequency content of the RF pulses^{43,44} (Extended Data Fig. 8).

In STM-based approaches, tunneling electrons have posed severe limitations on the energy relaxation time T_1 and coherence time T_2 of the spins^{30,45}. This limitation is overcome in our scheme because tunneling electrons pass only through the sensor qubit and do not flow through the remote qubits (Fig. 1a). To characterize the remote qubits, we first perform an inversion recovery measurement⁴⁶ to obtain an energy relaxation time $T_1 = 166 \pm 14$ ns¹². A pronounced improvement is seen in the quantum coherence of remote qubits, which is already visible in the higher quality of the remote qubit's Rabi oscillations (Fig. 3a) compared to the sensor qubit (Fig. 3c and 3d). Figure 5b shows the Ramsey signal measured at a tunnel current of $I_{DC} = 10$ pA, from which we extract a coherence time $T_2^* = 86 \pm 13$ ns. We find that T_2^* , the coherence time subject to inhomogeneous broadening, depends on the tunnel current and hence on the tip height (Fig. 5b

inset, Extended Data Fig. 5a), suggesting that the proximity of the STM tip to the remote qubits influences their quantum coherence time despite the absence of tunnel current. This decoherence effect is likely due to field fluctuations arising from slight, uncontrolled tip motions⁴⁵. To cancel the effect of this inhomogeneous broadening, we perform a spin-echo measurement and observe that the measured T_2^{Echo} shows negligible dependence on the tunnel current (Fig. 5c inset and Extended Data Fig. 5b). The measured coherence time $T_2^{\text{Echo}} = 300 \pm 54$ ns (Fig. 5c) strikingly approaches the theoretical limit of $2T_1$. These measurements highlight that the quantum coherence of remote qubits after spin-echo filtering is limited by energy relaxation events, in contrast to other solid-state qubits, where $T_1 \gg T_2^{\text{Echo}}$ usually applies.

Further increases in T_1 and T_2^{Echo} should be possible by use of thicker insulating layers to better isolate the qubits from substrate electrons and by switching to longer-lived single-atom magnets such as Ho and Dy^{16,17,47}. The remote qubits can in principle be positioned on a fully insulating material as long as they couple to the sensor spin placed on a weakly conductive region of the surface. A variety of material systems, such as those involving two-dimensional heterostructures, offer such possibilities^{48,49}.

We have shown the atom-by-atom fabrication and coherent manipulation of a novel electron-spin qubit platform. Coherently controlling multiple qubits with a single STM tip overcomes a previous limitation in STM-based quantum control schemes. A unique benefit of our surface-based electron-spin approach is the myriad of available spin species^{28,50} and the vast variety of two-dimensional geometries that can be controllably assembled. We anticipate that multi-spin entanglement demonstration⁵¹, quantum computation⁵², sensing⁵³ and simulation⁵⁴ protocols using an atomic architecture on a surface can now be attempted.

Acknowledgments

We thank A. Ardavan, M. Ternes, J. F. Rossier, D. Loss, F. Donati, and F. Cho for fruitful discussions. This work was supported by the Institute for Basic Science (IBS-R027-D1). C.P.L. acknowledges support from the Office of Naval Research, grant N00014-21-1-2467. M.H. acknowledges financial support from University of Tokyo Global Activity Support Program for Young Researchers (FY2020). D.-J.C. and C.M. acknowledge funding from the Spanish State Research Agency grants (RTI2018-097895-B-C44, Excelencia EUR2020-112116 and PID2021-127917NB-I00) funded by MCIN/AEI/10.13039/501100011033 and by "ERDF A way of making Europe", and Eusko Jauriaritza (project PIBA 2020_1_0017).

Author contributions

A.J.H., S.P., and C.P.L. conceived the project. Y.W., Y.C., H.T.B., M.H., C.M., J.K., D.-J.C., Y.B., and S.P. performed the measurements and data analysis. C.W. carried out simulations to optimize the measurement schemes. All authors discussed and prepared the manuscript together.

Competing interests

The authors declare no competing interests.

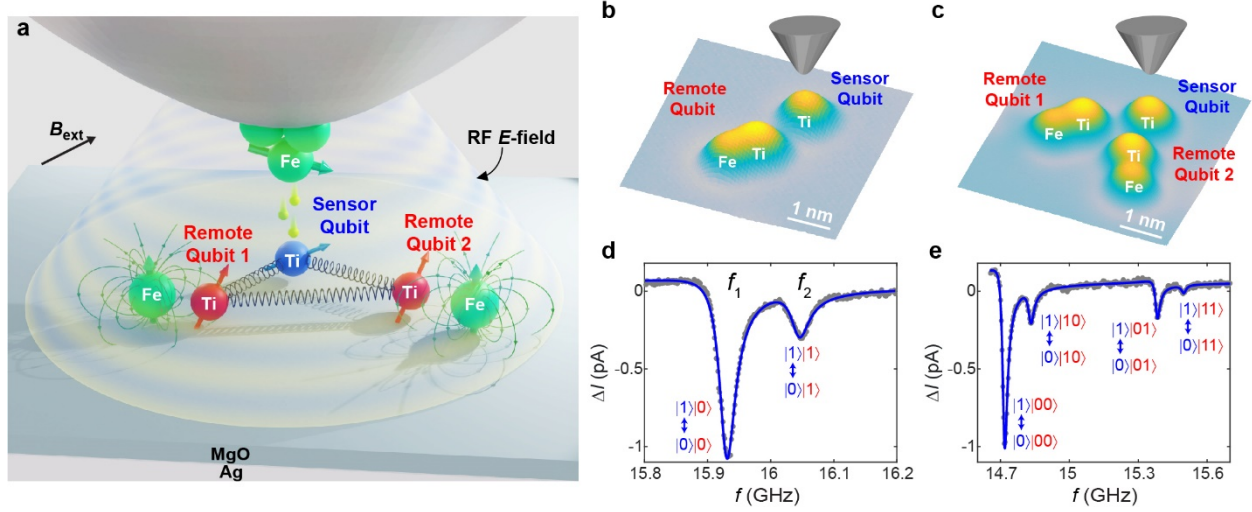


Fig. 1 | Bottom-up construction of multiple coupled electron spin qubits. **a**, Schematic: A sensor spin qubit (Ti, blue) is placed under the apex of a spin-polarized STM tip for readout. Remote qubits are constructed at precise separations to the sensor qubit by atom manipulations. Each remote qubit is composed of a spin-1/2 Ti atom (red) and a single-atom magnet (Fe) (green), where Fe's magnetic field gradient, in combination with the RF electric field between the tip and the sample, coherently drives remote qubits. **b,c**, Constant-current STM images showing atom-by-atom construction of a multi-qubit structure (image size: $5.0 \text{ nm} \times 5.0 \text{ nm}$). **d,e**, Continuous-wave ESR spectra measured with the tip positioned on the sensor qubit in the structures shown in **b** and **c**. Each ESR resonance of the sensor qubit distinguishes a quantum state of the remote qubits (red kets). The quantum states of the sensor qubit are labeled by blue kets. Imaging conditions in **b** and **c**: sample bias voltage $V_{DC} = 100 \text{ mV}$, time-averaged tunnel current $I_{DC} = 10 \text{ pA}$. ESR conditions in **d** and **e**: $V_{DC} = 50 \text{ mV}$, $I_{DC} = 20 \text{ pA}$, zero-to-peak RF voltage $V_{RF} = 30 \text{ mV}$.

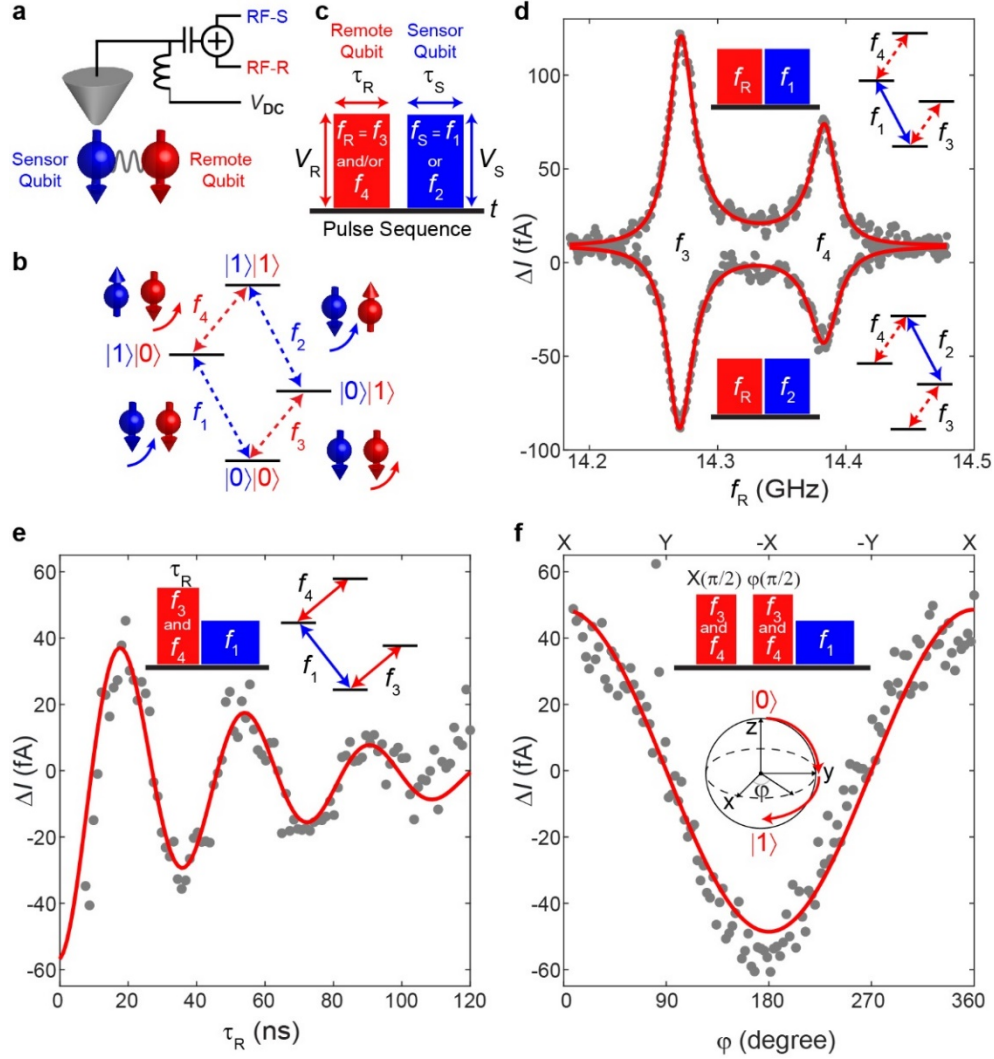


Fig. 2 | Coherent control of a single remote qubit. **a**, Schematic of the measurement scheme. Two RF tones, RF-S and RF-R, are applied to the STM tip for the coherent control of the sensor and remote qubit, respectively. The atomic structure used in this figure is shown in Fig. 1b. **b**, Energy diagram and ESR transitions of the two-qubit system. **c**, Typical pulse sequence composed of a control pulse on the remote qubit (red) followed by a sensing pulse on the sensor qubit (blue). The control pulse can induce conditional or unconditional qubit rotations depending on its frequency content. **d**, ESR spectra of the remote qubit measured with the tip positioned on the sensor qubit. The two curves in **d** correspond to different sensing frequencies (upper: $f_s = f_1$, lower: $f_s = f_2$). Insets: pulse sequence and ESR transitions involved in each spectrum. **e**, Rabi oscillations of the remote qubit performed by simultaneously driving $f_R = f_3$ and f_4 to induce unconditional qubit rotations. The sensing pulse is subsequently applied at $f_s = f_1$. Red curve is a fit to an exponentially decaying sinusoid. **f**, Two-axis control of the remote qubit shown by sweeping the relative phase ϕ between two $\pi/2$ pulses ($f_R = f_3$ and f_4 ; $f_s = f_1$). Solid curve shows a cosine fit. The trajectory of the remote qubit is illustrated by red arrows on the Bloch sphere in the rotating frame. ESR conditions in **d**: $V_{DC} = 50$ mV, $I_{DC} = 20$ pA, $V_S = V_R = 30$ mV, $\tau_R = \tau_S = 200$ ns. **e** and **f**: $V_{DC} = 50$ mV, $I_{DC} = 20$ pA, $V_S = 50$ mV, $V_R = 120$ mV, $\tau_S = 200$ ns.

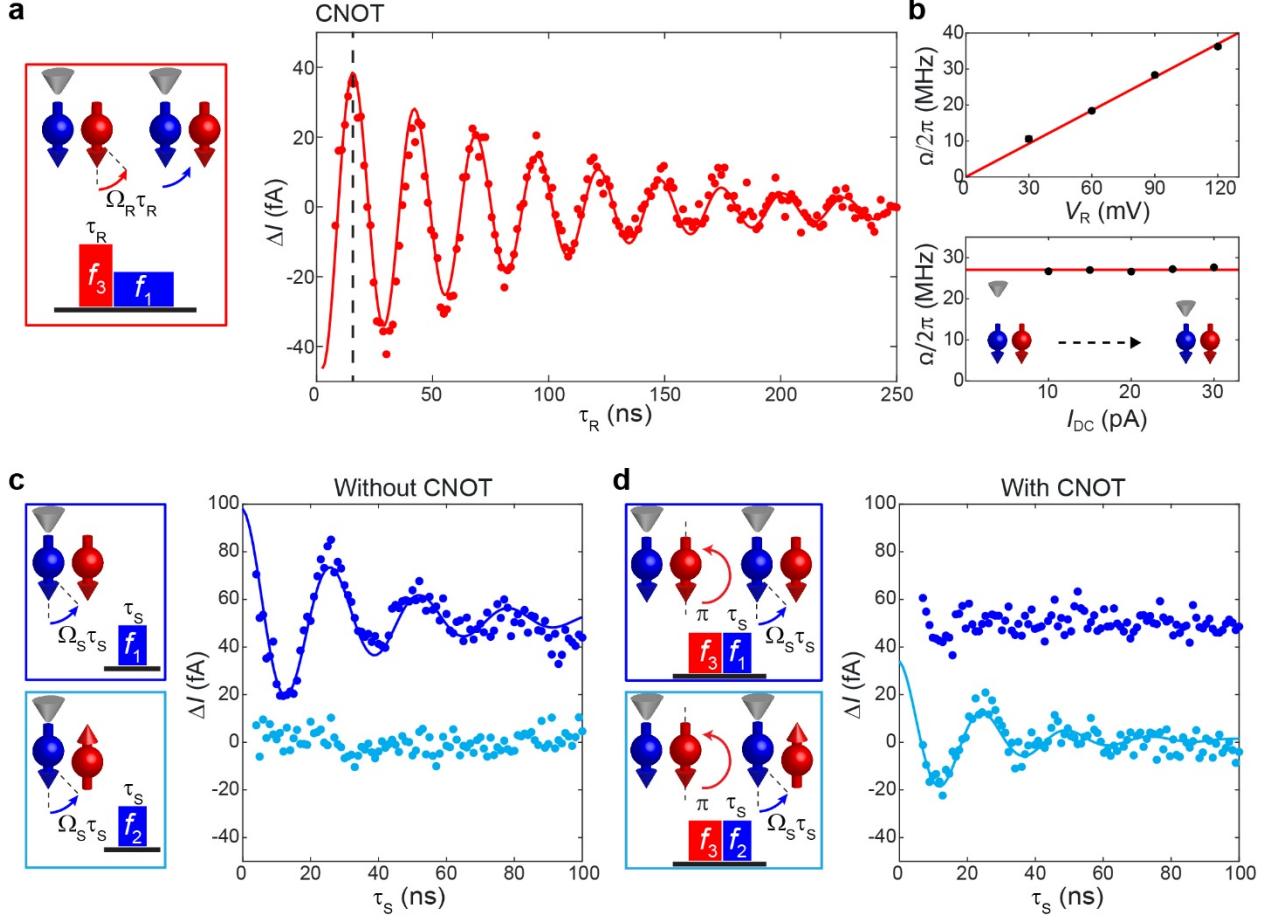


Fig. 3 | Two-qubit operations in the coupled-qubit structure shown in Fig. 1b. **a**, Controlled rotation of the remote qubit, conditional on the sensor qubit state being $|0\rangle$, obtained by driving the transition $|0\rangle|0\rangle \leftrightarrow |0\rangle|1\rangle$ at $f_R = f_3$. Red points show coherent oscillations of the remote qubit detected through a sensing pulse at $f_S = f_1$, as shown schematically on the left. Red curve is a decaying sinusoidal fit. The CNOT operation time is ~ 13 ns (dotted line). **b**, The rate of controlled rotations, $\Omega/2\pi$, of the remote qubit. The rate increases linearly with the RF voltage V_R (upper) but remains unchanged as the tunnel current I_{DC} (lower) is varied. Error bars are comparable with the size of symbols. Solid curves are linear fits. Inset illustrates the change of tip-sensor separations. **c,d**, Controlled rotations of the sensor qubit without (c) and with (d) a CNOT operation at $f_R = f_3$ on the remote qubit. Blue (cyan) points measured with $f_S = f_1$ (f_2) show sensor Rabi oscillation (solid lines are decaying exponential fits) only when the remote qubit has a significant population in state $|0\rangle$ ($|1\rangle$). The CNOT operation transfers the predominant population from state $|0\rangle|0\rangle$ to state $|0\rangle|1\rangle$, thus causing the opposite trends of the oscillations in c and d. Blue curves are shifted vertically by 50 fA for clarity. ESR conditions in **a**: $V_{DC} = 50$ mV, $I_{DC} = 10$ pA, $V_S = 30$ mV, $V_R = 120$ mV, $\tau_S = 200$ ns. **c**: $V_{DC} = 20$ mV, $I_{DC} = 7.5$ pA, $V_S = 100$ mV. **d**: $V_{DC} = 20$ mV, $I_{DC} = 7.5$ pA, $V_S = V_R = 100$ mV.

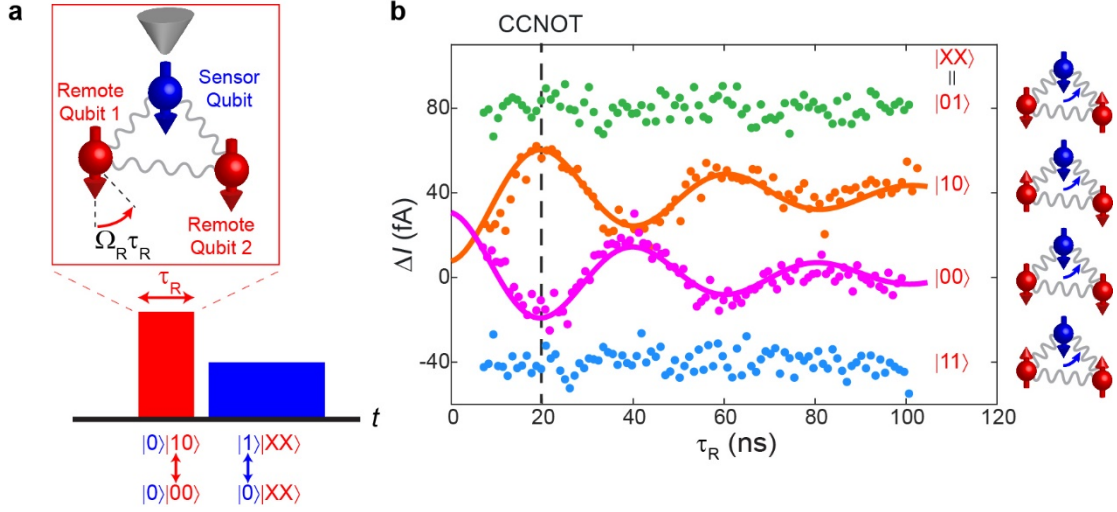


Fig. 4 | Three-qubit operations in a multi-qubit atomic structure. **a**, Schematic showing the control scheme of a multi-qubit structure (Fig. 1c) composed of two remote qubits and a sensor qubit. **b**, Controlled-controlled operation of remote qubit 1 performed by driving the transition $|0\rangle|00\rangle \leftrightarrow |0\rangle|10\rangle$ (red pulse in **a**). Four different frequencies of the sensor qubit are used for sensing the four remote qubit states (blue pulse in **a**, where the detected states of the remote qubits are labelled in red kets in **b**). The two oscillating curves in **b** (orange and magenta) correspond to detection of the remote qubits' $|00\rangle$ or $|10\rangle$ states upon the controlled-controlled operation at $|0\rangle|00\rangle \leftrightarrow |0\rangle|10\rangle$. The CCNOT operation time is ~ 20 ns (dotted line). The other two qubit states are nearly unoccupied so they show no clear oscillations. Green, orange and blue curves are vertically shifted for clarity. ESR conditions in **b**: $V_{DC} = 50$ mV, $I_{DC} = 20$ pA, $V_S = 50$ mV, $V_R = 80$ mV, $\tau_S = 200$ ns.

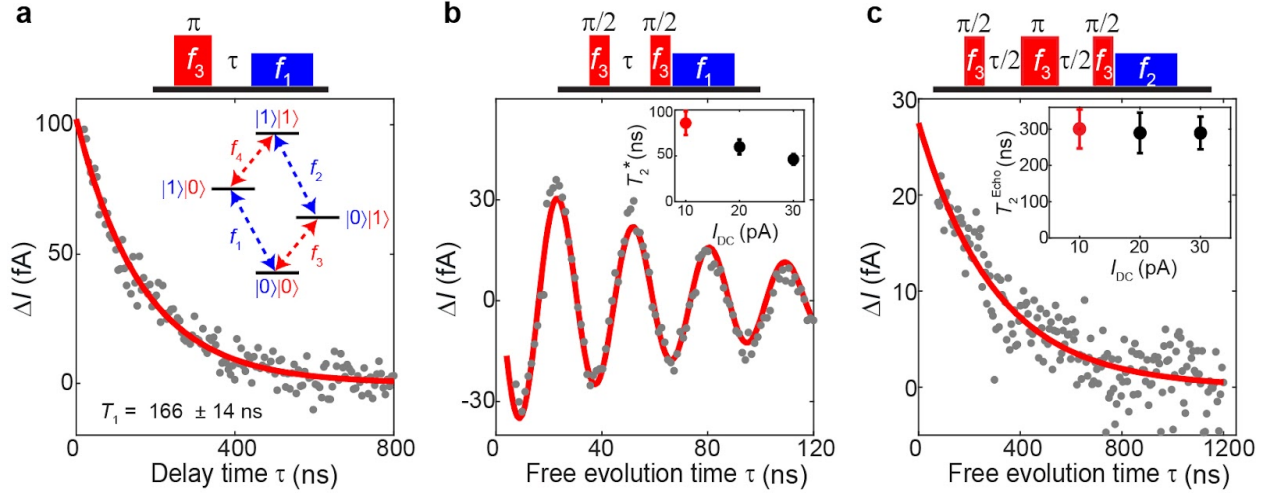


Fig. 5 | Relaxation and coherence properties of remote qubits. The two-qubit structure shown in Fig. 1b is used in these measurements. **a**, Relaxation time T_1 of the remote qubit measured by an inversion recovery scheme. The exponential fit (solid line) yields a relaxation time T_1 of 166 ± 14 ns for the remote qubit. Inset: Labels of ESR transitions used in this figure (same as Fig. 2b). **b**, Ramsey measurements of the remote qubit with $f_S = f_1$ and $f_R = f_3 + 30$ MHz yielding a coherence time $T_2^* = 86 \pm 13$ ns. Inset: T_2^* shows a weak dependence on the tunnel current I_{DC} . **c**, Spin-echo measurements of the remote qubit measured with $f_S = f_2$ and $f_R = f_3$. The exponential fit (solid line) yields a coherence time of $T_2^{\text{Echo}} = 300 \pm 54$ ns. Inset: T_2^{Echo} shows no dependence on I_{DC} . ESR conditions in **a**: $V_{DC} = 50$ mV, $I_{DC} = 20$ pA, $V_S = 50$ mV, $V_R = 120$ mV, $\tau_S = 200$ ns. **b** and **c**: $V_{DC} = 50$ mV, $I_{DC} = 10$ pA, $V_S = 60$ mV, $V_R = 120$ mV, $\tau_S = 200$ ns.

References

- 1 Feynman, R. P. Simulating physics with computers. *International Journal of Theoretical Physics* **21**, 467–488, doi:10.1007/BF02650179 (1982).
- 2 Feynman, R. P. There's plenty of room at the bottom. *Engineering and science* **23**, 22-36 (1960).
- 3 Zwanenburg, F. A., Dzurak, A. S., Morello, A., Simmons, M. Y., Hollenberg, L. C. L., Klimeck, G., Rogge, G., Coppersmith, S. N., Eriksson, M. A. Silicon quantum electronics. *Reviews of Modern Physics* **85**, 961–1019, doi:10.1103/RevModPhys.85.961 (2013).
- 4 Awschalom, D. D., Hanson, R., Wrachtrup, J. & Zhou, B. B. Quantum technologies with optically interfaced solid-state spins. *Nature Photonics* **12**, 516–527, doi:10.1038/s41566-018-0232-2 (2018).
- 5 Morello, A., Pla, J. J., Zwanenburg, F. A., Chan, K. W., Tan, K. Y., Huebl, H., Mottonen, M., Nugroho, C. D., Yang, C., van Donkelaar, J. A., Alves, A. D. C., Jamieson, D. N., Escott, C. C., Hollenberg, L. C. L., Clark, R. G., Dzurak, A. S. Single-shot readout of an electron spin in silicon. *Nature* **467**, 687-691, doi:10.1038/nature09392 (2010).
- 6 He, Y., Gorman, S. K., Keith, D., Kranz, L., Keizer, J. G., Simmons M. Y. A two-qubit gate between phosphorus donor electrons in silicon. *Nature* **571**, 371-375, doi:10.1038/s41586-019-1381-2 (2019).
- 7 Borjans, F., Croot, X. G., Mi, X., Gullans, M. J. & Petta, J. R. Resonant microwave-mediated interactions between distant electron spins. *Nature* **577**, 195-198, doi:10.1038/s41586-019-1867-y (2020).
- 8 Pompili, M., Hermans, S. L. N., Baier, S., Beukers, H. K. C., Humphreys, P. C., Schouten, R. N., Vermeulen, R. F. L., Tiggelman, M. J., dos Santos Martins, L., Dirkse, B., Wehner, S., Hanson, R. Realization of a multinode quantum network of remote solid-state qubits. *Science* **372**, 259-264, doi:doi:10.1126/science.abg1919 (2021).
- 9 Choi, D.-J., Lorente, N., Wiebe, J., von Bergmann, K., Otte, A. F., Heinrich, A. J. Colloquium: Atomic spin chains on surfaces. *Reviews of Modern Physics* **91**, doi:10.1103/RevModPhys.91.041001 (2019).
- 10 Baumann, S. Paul, W., Choi, T., Lutz, C. P., Ardavan, A., Heinrich, A. J. Electron paramagnetic resonance of individual atoms on a surface. *Science* **350**, 417-420 (2015).
- 11 Bae, Y., Yang, K., Willke, P., Choi, T., Heinrich, A. J., Lutz, C. P. Enhanced quantum coherence in exchange coupled spins via singlet-triplet transitions. *Science advances* **4**, eaau4159 (2018).
- 12 Veldman, L. M., Farinacci, L., Rejali, R., Broekhoven, R., Gobeil, J., Coffey, D., Ternes, M., Otte, A. F. Free coherent evolution of a coupled atomic spin system initialized by electron scattering. *Science* **372**, 964-968 (2021).
- 13 Imada, H., Miwa, K., Imai-Imada, M., Kawahara, S., Kimura, K., Kim, Y. Real-space investigation of energy transfer in heterogeneous molecular dimers. *Nature* **538**, 364-367, doi:10.1038/nature19765 (2016).
- 14 Yang, K., Paul, W., Phark, S. H., Willke, P., Bae, Y., Choi, T., Esat, T., Ardavan, A., Heinrich, A. J., Lutz, C. P. Coherent spin manipulation of individual atoms on a surface. *Science* **366**, 509-512 (2019).
- 15 Willke, P., Bilgeri, T., Zhang, X., Wang, Y., Wolf, C., Aubin, H., Heinrich, A. J., Choi, T. Coherent Spin Control of Single Molecules on a Surface. *ACS Nano*, doi:10.1021/acsnano.1c06394 (2021).

- 16 Donati, F., Rusponi, S., Stepanow, S., Wäckerlin, C., Singha, A., Persichetti, L., Baltic, R., Diller, K., Patthey, F., Fernandes, E., Dreiser, J., Šljivančanin, Ž., Kummer, K., Nistor, C., Gambardella, P., Brune, H. Magnetic remanence in single atoms. *Science* **352**, 318-321 (2016).
- 17 Natterer, F. D., Yang, K., Paul, W., Willke, P., Choi, T., Greber, T., Heinrich, A. J., Lutz, C. P. Reading and writing single-atom magnets. *Nature* **543**, 226-228, doi:10.1038/nature21371 (2017).
- 18 Heinrich, A. J., Oliver, W. D., Vandersypen, L., Ardavan, A., Sessoli, R., Loss, D., Jayich, A. B., Fernandez-Rossier, J., Laucht, A., Morello, A. Quantum-coherent nanoscience. *Nat Nanotechnol* **16**, 1318-1329, doi:10.1038/s41565-021-00994-1 (2021).
- 19 Thiele, S., Balestro, F., Ballou, R., Klyatskaya, S., Ruben, M., Wernsdorfer, W. Electrically driven nuclear spin resonance in single-molecule magnets. *Science* **344**, 1135-1138 (2014).
- 20 Wang, L., Xia, Y., Ho, W. Atomic-scale quantum sensing based on the ultrafast coherence of an H₂ molecule in an STM cavity. *Science* **376**, 401-405, doi:10.1126/science.abn9220 (2022).
- 21 Eigler, D. M. & Schweizer, E. K. Positioning single atoms with a scanning tunnelling microscope. *Nature* **344**, 524-526 (1990).
- 22 Khajetoorians, A. A., Wegner, D., Otte, A. F. & Swart, I. Creating designer quantum states of matter atom-by-atom. *Nature Reviews Physics* **1**, 703-715 (2019).
- 23 Kiczynski, M., Gorman, S. K., Geng, H., Donnelly, M. B., Chung, Y., He, Y., Keizer, J. G., Simmons, M. Y. Engineering topological states in atom-based semiconductor quantum dots. *Nature* **606**, 694-699, doi:10.1038/s41586-022-04706-0 (2022).
- 24 Seifert, T. S., Kovarik, S., Juraschek, D. M., Spaldin, N. A., Gambardella, P., Stepanow, S. Longitudinal and transverse electron paramagnetic resonance in a scanning tunneling microscope. *Science advances* **6**, eabc5511 (2020).
- 25 Steinbrecher, M., van Weerdenburg, W. M. J., Walraven, E. F., van Mullekom, N. P. E., Gerritsen, J. W., Natterer, F. D., Badrtdinov, D. I., Rudenko, A. N., Mazurenko, V. V., Vladimir, V., Katsnelson, M. I., van der Avoird, A., Groenenboom, G. C., Khajetoorians, A. Quantifying the interplay between fine structure and geometry of an individual molecule on a surface. *Physical Review B* **103**, doi:10.1103/PhysRevB.103.155405 (2021).
- 26 Kim, J., Jang, W., Bui, H. T., Choi, D., Wolf, C., Delgado, F., Krylov, D., Lee, S., Yoon, S., Lutz, C. P., Heinrich, A. J., Bae, Y. Spin resonance amplitude and frequency of a single atom on a surface in a vector magnetic field. *Physical Review B* **104**, doi:10.1103/PhysRevB.104.174408 (2021).
- 27 Zhang, X., Wolf, C., Wang, Y., Aubin, H., Bilgeri, T., Willke, P., Heinrich, A. J., Choi, T. Electron spin resonance of single iron phthalocyanine molecules and role of their non-localized spins in magnetic interactions. *Nat Chem* **14**, 59-65, doi:10.1038/s41557-021-00827-7 (2022).
- 28 Chen, Y., Bae, Y. & Heinrich, A. J. Harnessing the Quantum Behavior of Spins on Surfaces. *Advanced Materials*, 2107534 (2022).
- 29 Yang, K., Bae, Y., Paul, W., Natterer, F. D., Willke, P., Lado, J. L., Ferrón, A., Choi, T., Fernández-Rossier, J., Heinrich, A. J., Lutz, C. P. Engineering the Eigenstates of Coupled Spin-1/2 Atoms on a Surface. *Phys Rev Lett* **119**, 227206, doi:10.1103/PhysRevLett.119.227206 (2017).

- 30 Paul, W., Yang, K., Baumann, S., Romming, N., Choi, T., Lutz, C. P., Heinrich, A. J. Control of the millisecond spin lifetime of an electrically probed atom. *Nature Physics* **13**, 403-407, doi:10.1038/nphys3965 (2016).
- 31 Lado, J. L., Ferrón, A. & Fernández-Rossier, J. Exchange mechanism for electron paramagnetic resonance of individual adatoms. *Physical Review B* **96**, doi:10.1103/PhysRevB.96.205420 (2017).
- 32 Yang, K., Paul, W., Natterer, F. D., Lado, J. L., Bae, Y., Willke, P., Choi, T., Ferrón, A., Fernández-Rossier, J., Heinrich, A. J., Lutz, C. P. Tuning the Exchange Bias on a Single Atom from 1 mT to 10 T. *Phys Rev Lett* **122**, 227203, doi:10.1103/PhysRevLett.122.227203 (2019).
- 33 Tokura, Y., van der Wiel, W. G., Obata, T. & Tarucha, S. Coherent single electron spin control in a slanting Zeeman field. *Phys Rev Lett* **96**, 047202, doi:10.1103/PhysRevLett.96.047202 (2006).
- 34 Koiller, B., Hu, X. & Das Sarma, S. Exchange in silicon-based quantum computer architecture. *Phys Rev Lett* **88**, 027903, doi:10.1103/PhysRevLett.88.027903 (2002).
- 35 Kevan, L. & Kispert, L. D. *Electron Spin Double Resonance Spectroscopy*. (Wiley, 1976).
- 36 Kawakami, E., Scarlino, P., Ward, D. R., Braakman, F. R., Savage, D. E., Lagally, M. G., Friesen, M., Coppersmith, S. N., Eriksson, M. A., Vandersypen, L. M. K. Electrical control of a long-lived spin qubit in a Si/SiGe quantum dot. *Nat Nanotechnol* **9**, 666-670, doi:10.1038/nnano.2014.153 (2014).
- 37 Wolfowicz, G. & Morton, J. J. L., Pulse Techniques for Quantum Information Processing, *eMagRes* **5**, 1515-1528, doi:10.1002/9780470034590.emrstm1521 (2016).
- 38 Huang, W., Yang, C. H., Chan, K. W., Tanttu, T., Hensen, B., Leon, R. C. C., Fogarty, M. A., Hwang, J. C. C., Hudson, F. E., Itoh, K. M., Morello, A., Laucht, A., Dzurak, A. S. Fidelity benchmarks for two-qubit gates in silicon. *Nature* **569**, 532-536, doi:10.1038/s41586-019-1197-0 (2019).
- 39 Hendrickx, N. W., Franke, D. P., Sammak, A., Scappucci, G. & Veldhorst, M. Fast two-qubit logic with holes in germanium. *Nature* **577**, 487-491, doi:10.1038/s41586-019-1919-3 (2020).
- 40 DiVincenzo, D. P. Two-bit gates are universal for quantum computation. *Physical Review A* **51**, 1015 (1995).
- 41 Reed, M. D., DiCarlo, L., Nigg, S. E., Sun, L., Frunzio, L., Girvin, S. M., Schoelkopf, R. J. Realization of three-qubit quantum error correction with superconducting circuits. *Nature* **482**, 382-385, doi:10.1038/nature10786 (2012).
- 42 Monz, T., Kim, K., Hänsel, W., Riebe, M., Villar, A. S., Schindler, P., Chwalla, M., Hennrich, M., Blatt, R. Realization of the quantum Toffoli gate with trapped ions. *Phys Rev Lett* **102**, 040501, doi:10.1103/PhysRevLett.102.040501 (2009).
- 43 Vandersypen, L. M. K., Steffen, M., Breyta, G., Yannoni, C. S., Sherwood, M. H., Chuang, I. L. Experimental realization of Shor's quantum factoring algorithm using nuclear magnetic resonance. *Nature* **414**, 883-887 (2001).
- 44 Vandersypen, L. M. & Chuang, I. L. NMR techniques for quantum control and computation. *Reviews of modern physics* **76**, 1037 (2005).
- 45 Willke, P., Paul, W., Natterer, F. D., Yang, K., Bae, Y., Choi, T., Fernández-Rossier, J., Heinrich, A. J., Lutz, C. P. Probing quantum coherence in single-atom electron spin resonance. *Science advances* **4**, eaaq1543 (2018).

- 46 Jacobsen, N. E. *NMR spectroscopy explained: simplified theory, applications and examples for organic chemistry and structural biology*. (John Wiley & Sons, 2007).
- 47 Singha, A., Willke, P., Bilgeri, T., Zhang, X., Brune, H., Donati, F., Heinrich, A. J., Choi, T. Engineering atomic-scale magnetic fields by dysprosium single atom magnets. *Nature Communications* **12**, 1-6 (2021).
- 48 Yang, W., Chen, G., Shi, Z., Liu, C., Zhang, L., Xie, G., Cheng, M., Wang, D., Yang, R., Shi, D., Watanabe, K., Taniguchi, T., Yao, Y., Zhang, Y., Zhang, G. Epitaxial growth of single-domain graphene on hexagonal boron nitride. *Nat Mater* **12**, 792-797, doi:10.1038/nmat3695 (2013).
- 49 Wang, P., Lee, W., Corbett, J. P., Koll, W. H., Vu, N. M., Laleyan, D. A., Wen, Q., Wu, Y., Pandey, A., Gim, J., Wang, D., Qiu, D. Y., Hovden, R., Kira, M., Heron, J. T., Gupta, J. A. Emmanouil Kioupakis, Zetian Mi. Scalable Synthesis of Monolayer Hexagonal Boron Nitride on Graphene with Giant Bandgap Renormalization. *Adv Mater* **34**, e2201387, doi:10.1002/adma.202201387 (2022).
- 50 Kovarik, S., Robles, R., Schlitz, R., Seifert, T. S., Lorente, N., Gambardella, P., Stepanow, S. Electron Paramagnetic Resonance of Alkali Metal Atoms and Dimers on Ultrathin MgO. *Nano Lett* **22**, 4176-4181, doi:10.1021/acs.nanolett.2c00980 (2022).
- 51 Neumann, P., Kolesov, R., Naydenov, B., Beck, J., Rempp, F., Steiner, M., Jacques, V., Balasubramanian, G., Markham, M. L., Twitchen, D. J., Pezzagna, S., Meijer, J., Twamley, J., Jelezko, F., Wrachtrup, J. Quantum register based on coupled electron spins in a room-temperature solid. *Nature Physics* **6**, 249-253, doi:10.1038/nphys1536 (2010).
- 52 DiVincenzo, D. P. The physical implementation of quantum computation. *Fortschritte der Physik: Progress of Physics* **48**, 771-783 (2000).
- 53 Degen, C. L., Reinhard, F. & Cappellaro, P. Quantum sensing. *Reviews of Modern Physics* **89**, doi:10.1103/RevModPhys.89.035002 (2017).
- 54 Trabesinger, A. Quantum simulation. *Nature Physics* **8**, 263-263, doi:10.1038/nphys2258 (2012).

Methods

Experimental setup

Experiments were performed with a commercial STM (Unisoku, USM1300) operating at 0.4 K. Two radio frequency (RF) generators (Agilent E8257D and E8267D) were combined by an RF power combiner. The combined RF signal was added to the DC bias voltage V_{DC} through a diplexer at room temperature and then applied to the STM tip. Both RF generators were gated by an arbitrary waveform generator (AWG, Tektronix 5000). The gating of the vector RF generator (E8267D) was performed by connecting two analog output channels of the AWG to the generator's in-phase and quadrature (I and Q) ports in order to control the phase of the RF pulses and drive multiple frequencies. The tunnel current was sensed by a room-temperature electrometer (Femto DLPCA-200). During ESR measurements, the signals were chopped at 95 Hz and sent to a lock-in amplifier (Stanford Research Systems SR860) and recorded (National Instruments 6363). A vector magnetic field (0.6 – 0.7 T) was applied mainly in the sample plane, with an out-of-plane component adjusted between 0.1 and 0.3 T. The bias voltage V_{DC} refers to the sample voltage relative to the tip. The STM constant-current feedback loop was set to a low gain during the measurements.

Measurement schemes and data processing

Each data point in the figures corresponds to a data acquisition time of $\sim 1\text{--}2$ s, during which the pulse sequences were unchanged and the averaged output voltage from the lock-in amplifier was recorded. Each lock-in cycle (~ 10.5 ms) was divided into an A-subcycle (~ 5.25 ms) and a B-subcycle (~ 5.25 ms). Each pulse sequence was set to be roughly $1\ \mu\text{s}$ long to allow enough time for qubit relaxation before the start of the next sequence¹⁴. As a result, each lock-in subcycle was

filled with repeated identical sequences with roughly 5000 repetitions. The pulse sequences used in A-subcycles are illustrated in the figures. Schemes in B-subcycles are chosen to cancel linear backgrounds in the raw data, which are caused by RF-voltage-induced broadening of a nonlinear dI/dV spectrum (RF rectification effects)⁵⁵. Continuous-wave ESR spectra (Figs. 1d, 1e and Extended Data Figs. 1 and 2) as well as sensor qubit rotations (Fig. 3c) were collected with the RF voltage applied only in the A-subcycles and absent in the B-subcycles.

In this work, the remote measurement scheme reads out the z -projection of the quantum state of the remote qubits by detecting conditional spin rotations of the sensor qubit.

Coherent oscillations and Ramsey signals were fitted with a decaying sinusoidal function after subtracting a linear background. A constant current offset induced by remaining RF rectification effects was removed in Figs. 2f, 5a and 5c.

Sample preparation

An atomically clean Ag(100) substrate was prepared by alternating Ar⁺ sputtering and annealing cycles. MgO films were grown on the Ag substrate at 700 K by evaporating Mg in an O₂ atmosphere of 1.1×10^{-6} Torr. Fe and Ti atoms were deposited on pre-cooled MgO samples. All Ti atoms are believed to be hydrogenated^{11,29}. All experiments were performed on bilayer MgO on Ag as confirmed by I - z spectroscopy on Fe atoms³⁰.

STM tips used for data acquisition

Magnetic tips used for measurements were made by picking up ~4–6 Fe atoms from the MgO surface until the tips yielded good ESR signals on Ti atoms. Data shown in this Article were taken with five different tips. These tips had different strength of spin polarization as shown in Extended

Data Fig. 5. Tip-1 was used to collect the data in Fig. 3b and Extended Data Fig. 3; tip-2 was used to collect the data in Figs. 1d, 2d, 3a, 5b, 5c and Extended Data Figs. 1, 4 and 9; tip-3 was used to collect the data in Figs. 2e, 2f and 5a; tip-4 was used to collect the data in Figs. 3c, 3d and Extended Data Fig. 6; tip-5 was used to collect the data in Figs. 1e, 4b and Extended Data Figs. 2 and 7.

Atomic-scale fabrication of the qubit structures

The atomic qubit structures were fabricated using a combination of atom manipulation techniques. Fe atoms were vertically manipulated by picking up and dropping off the atoms using a sharp STM tip. Ti atoms were horizontally manipulated by placing the tip in front of Ti and approaching the tip to the surface. All procedures are described in Refs. ^{28,56}. We found that the optimal distance between Ti and Fe atoms in a remote qubit is ~ 0.6 nm (Fig. 1b and remote qubit 1 in Fig. 1c). A closer distance causes modifications of local density of states of Ti atoms, while a longer distance greatly reduces the remote driving strength. Atomically identical copies of each structure were created and showed no significant differences in ESR measurements.

Spin Hamiltonian

The static Hamiltonian of the qubit system shown in Fig. 1d can be written as

$$H = g\mu_B(\mathbf{B}_{\text{Fe}} + \mathbf{B}_{\text{ext}}) \cdot \mathbf{S}_R + g\mu_B(\mathbf{B}_{\text{tip}} + \mathbf{B}_{\text{ext}}) \cdot \mathbf{S}_S + J_{S-R} \mathbf{S}_S \cdot \mathbf{S}_R \\ + D(S_{S_z}S_{R_z} - \mathbf{S}_S \cdot \mathbf{S}_R)$$

where \mathbf{S}_S and \mathbf{S}_R are spin operators of the sensor and remote qubit, J and D are the exchange and dipolar coupling strengths, respectively. The couplings among sensor and remote qubits were

engineered by tuning their atomic separations and orientations (Extended Data Fig. 2). To separate the qubits' resonance frequencies, three strategies were used:

1. Adjusting the effective field \mathbf{B}_{Fe} from Fe atoms on remote Ti atoms, which is determined by their atomic separations and orientations on the MgO lattice.
2. Using different bridge binding-site orientations of Ti atoms on the MgO lattice because Ti atoms in different binding-sites yield different g -factors^{12,26}.
3. Changing the amplitude and direction of the external magnetic field \mathbf{B}_{ext} , which provides a global change of the qubit frequencies. In addition, different qubits' resonances shifted differently because of (1) their different g factors and (2) the presence of different \mathbf{B}_{Fe} (which is fixed in the out-of-plane direction⁵⁷ and barely affected by the external magnetic field).

Data availability

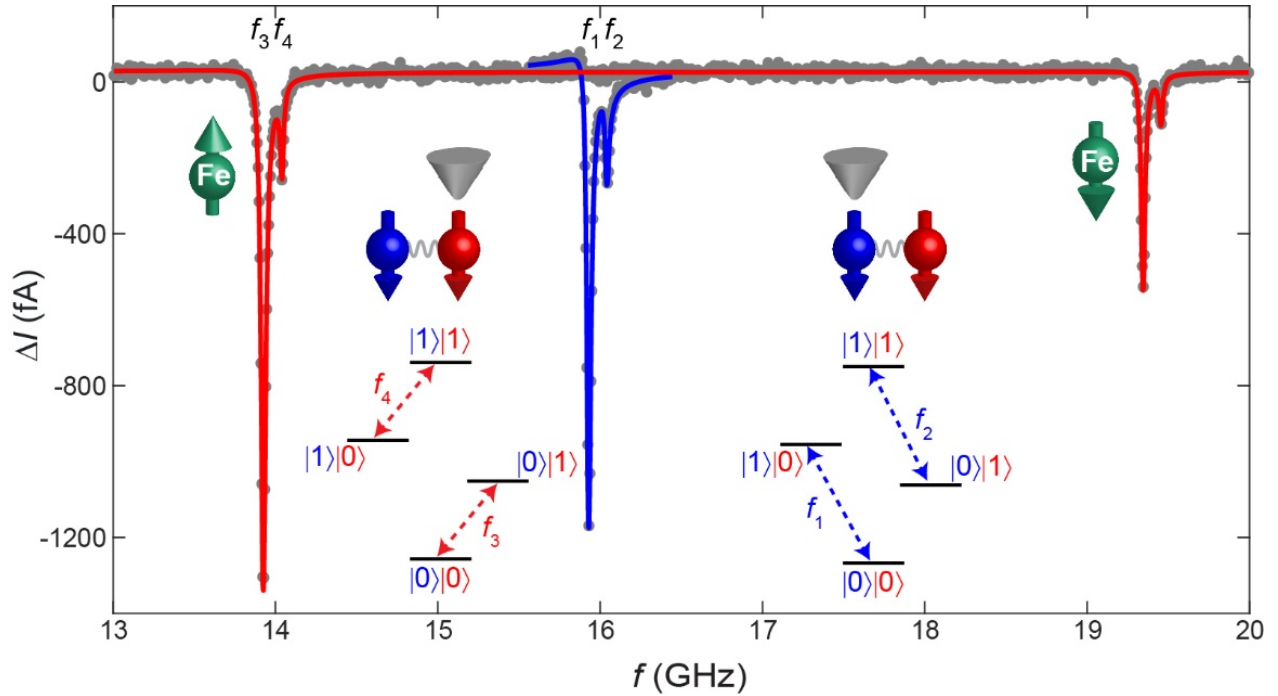
All data that support the plots within this paper and other findings of this study are available from the corresponding authors upon reasonable request.

Code availability

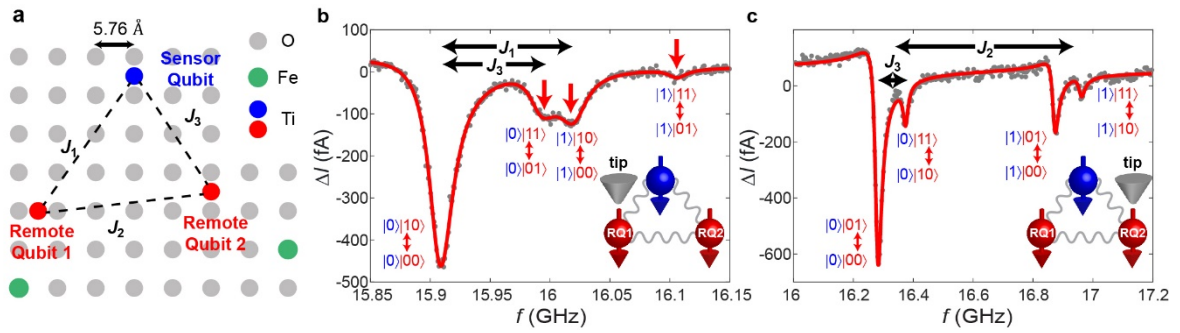
The codes used in this study are available from the corresponding authors upon reasonable request.

- 55 Paul, W., Baumann, S., Lutz, C. P. & Heinrich, A. J. Generation of constant-amplitude radio-frequency sweeps at a tunnel junction for spin resonance STM. *Rev Sci Instrum* **87**, 074703, doi:10.1063/1.4955446 (2016).
- 56 Yang, K., Phark, S. H., Bae, Y., Esat, T., Willke, P., Ardavan, A., Heinrich, A. J., Lutz, C. P. Probing resonating valence bond states in artificial quantum magnets. *Nat Commun* **12**, 993, doi:10.1038/s41467-021-21274-5 (2021).
- 57 Baumann, S., Donati, F., Stepanow, S., Rusponi, S., Paul, W., Gangopadhyay, S., Rau, I. G., Pacchioni, G. E., Gragnaniello, L., Pivetta, M., Dreiser, J., Piamonteze, C., Lutz, C. P.,

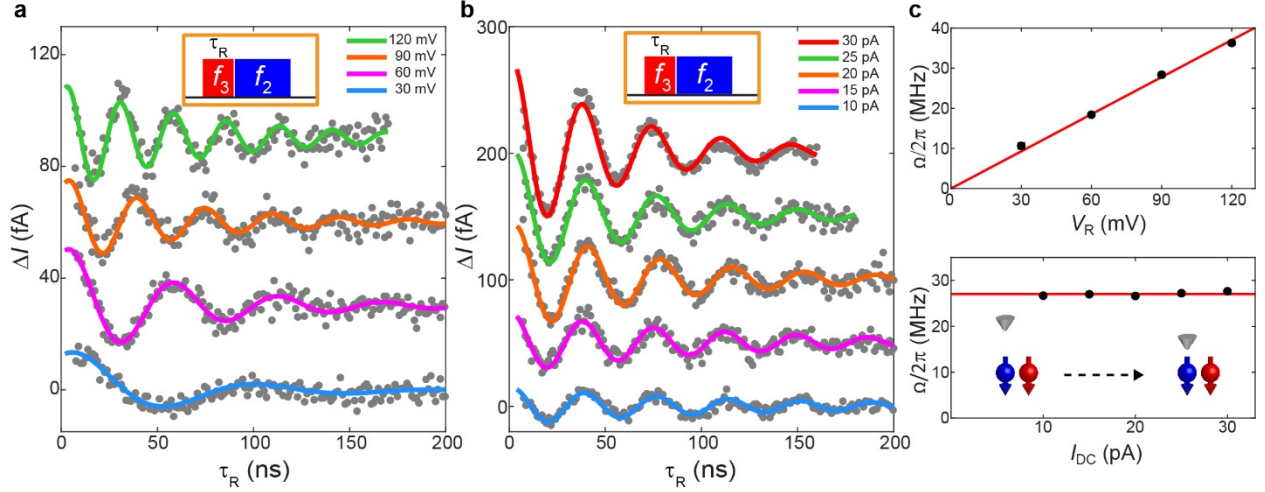
Macfarlane, R. M., Jones, B. A., Gambardella, P., Heinrich, A. J., Brune, H. Origin of Perpendicular Magnetic Anisotropy and Large Orbital Moment in Fe Atoms on MgO. *Physical Review Letters* **115**, 237202, doi:10.1103/PhysRevLett.115.237202 (2015).



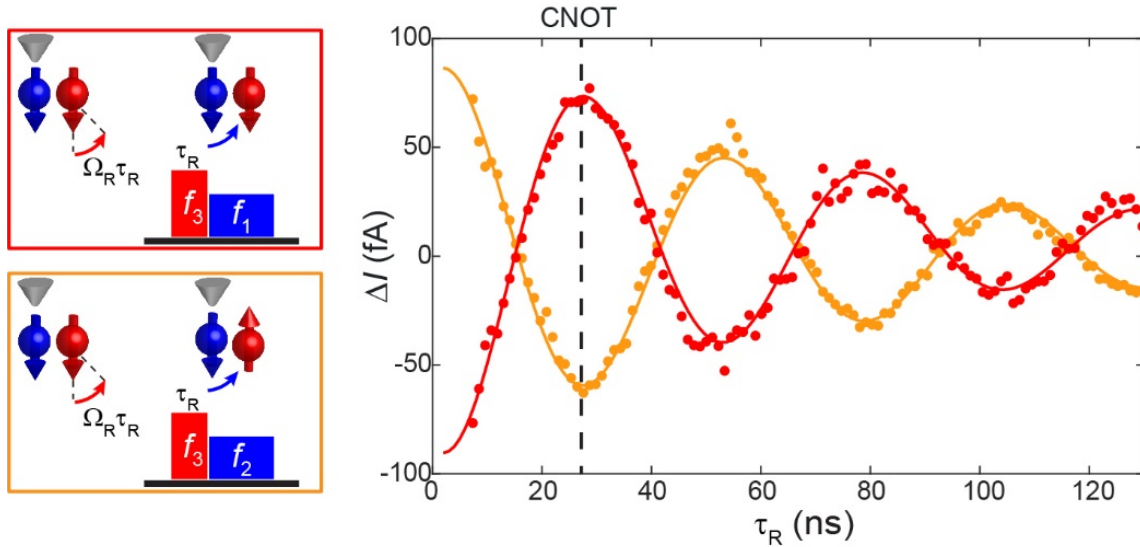
Extended Data Fig. 1 | Wide-range continuous-wave ESR spectra measured in the two-qubit structure shown in Fig. 1b. Unlike all spectra taken in the main text, where the STM tip is positioned only on the sensor qubit, the ESR spectra here are measured with the tip positioned either on the sensor qubit (blue) or on the “remote” qubit (red). The transitions corresponding to each ESR line are illustrated in the insets. Due to infrequent flipping of the Fe spin, the ESR spectrum measured on the remote qubit has two groups of peaks, corresponding to Fe’s spin up or down states. In this work, only ESR peaks at f_3 and f_4 (corresponding to Fe in the ground state $|\uparrow\rangle$) are considered because of their predominant strength. Fe flipping is expected to affect the spectra only slightly because Fe’s relaxation time is significantly longer than the timescale of each pulse sequence ($1 \mu\text{s}$)^{1,2}. ESR conditions: $V_{\text{DC}} = 50 \text{ mV}$, $I_{\text{DC}} = 20 \text{ pA}$, $V_{\text{RF}} = 30 \text{ mV}$.



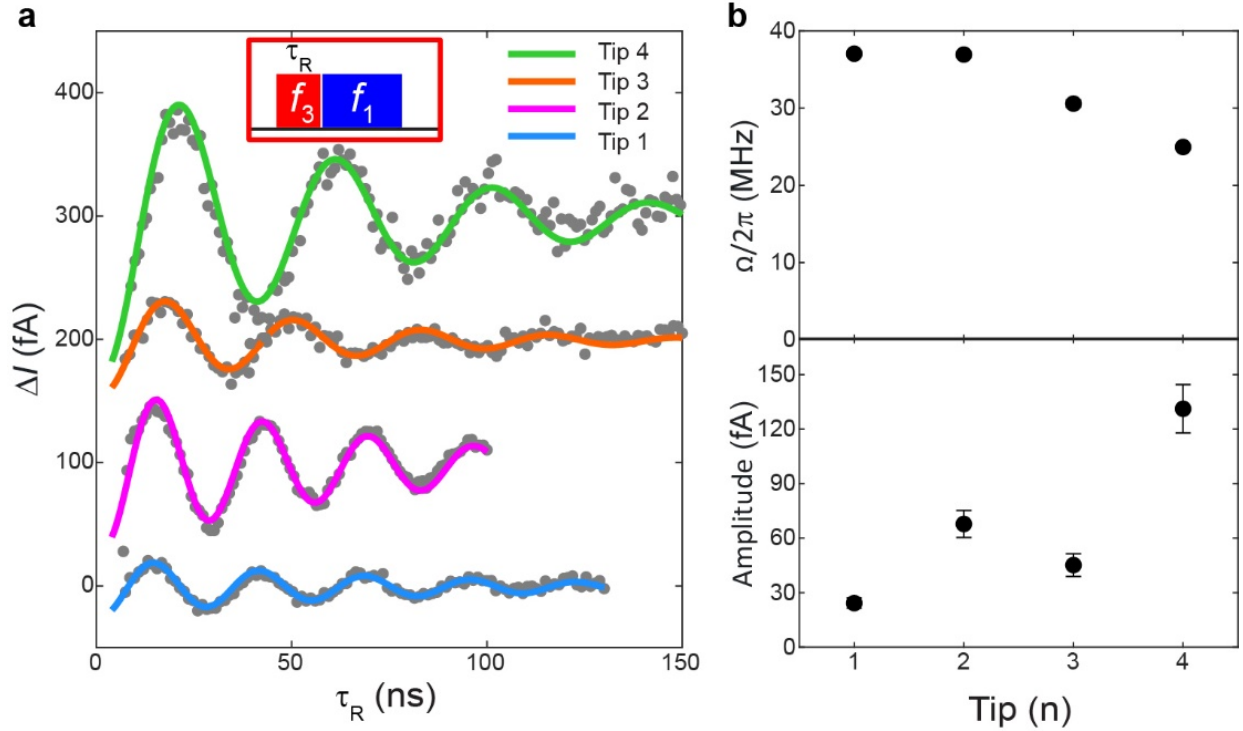
Extended Data Fig. 2 | Atomic registry of Ti and Fe atoms on the MgO lattice and continuous-wave ESR spectra of the three-qubit structure shown in Fig. 1c. **a**, Atomic registry of the three-qubit structure in Fig. 1c. The sensor Ti atom is shown in blue. In the remote qubits, Ti and Fe atoms are shown in red and green, respectively. Grey disks represent oxygen atoms. Fe atoms sit atop oxygen atoms, and Ti atoms sit at “bridge sites” between two oxygen atoms. The two-qubit structure in Fig. 1b has the same configuration but without remote qubit 2. **b,c**, Continuous-wave ESR spectra measured with the tip positioned on remote qubit 1 (RQ1) (b) and remote qubit 2 (RQ2) (c), as illustrated in the corresponding insets. The qubit-qubit interactions and transitions in each ESR spectrum are also labeled. From the ESR spectra we extract $J_1 = 113$ MHz, $J_2 = 59$ MHz, $J_3 = 88$ MHz. Signals corresponding to Fe’s excited spin state $|\downarrow\rangle$ are small and fall outside the frequency range shown here. ESR conditions in **b,c**: $V_{DC} = 50$ mV, $I_{DC} = 20$ pA, $V_{RF} = 30$ mV.



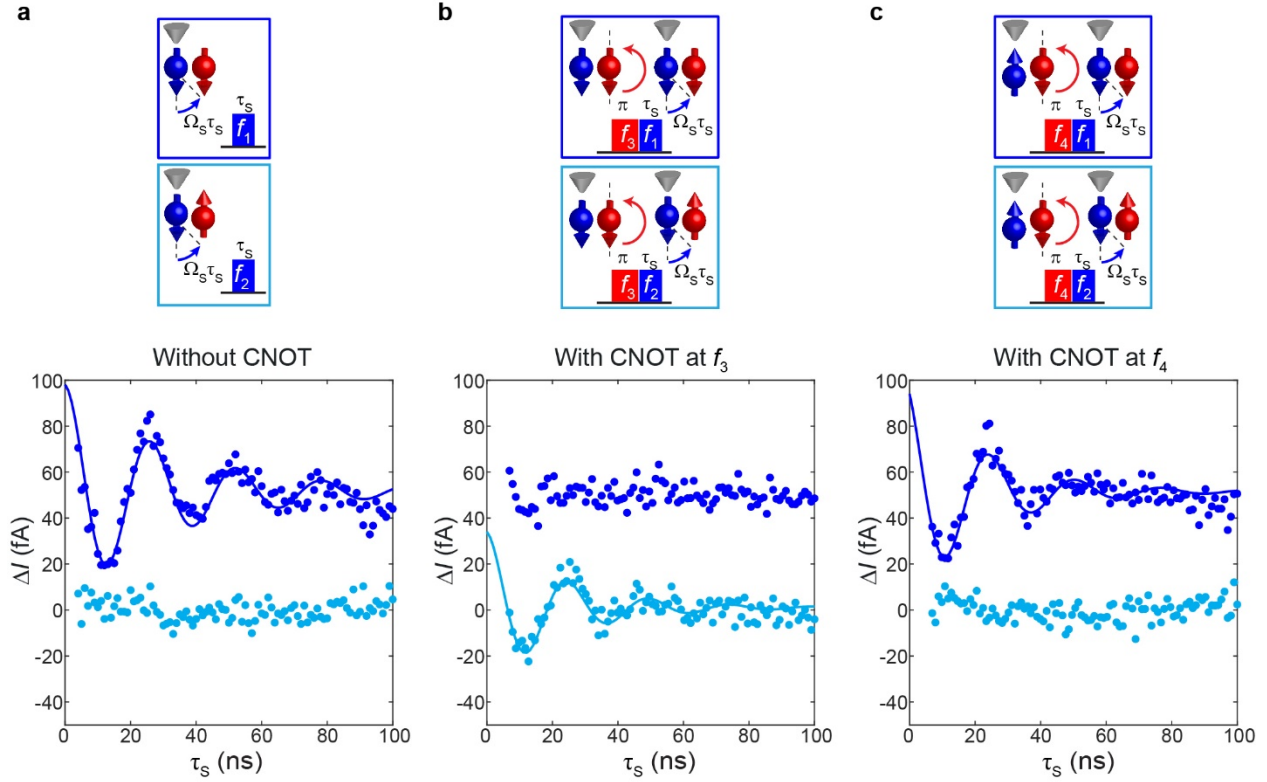
Extended Data Fig. 3 | Rates of controlled rotations of a remote qubit measured with varying parameters in the two-qubit structure shown in Fig. 1b. **a**, Controlled rotations of the remote qubit measured with varying RF driving voltage V_R (that acts on the remote qubit). The tunnel current is fixed at $I_{DC} = 20$ pA. **b**, Controlled rotations of the remote qubit measured at $V_R = 120$ mV with varying tunnel current I_{DC} . **c**, Extracted rates of controlled rotations, $\Omega/2\pi$, as functions of the RF driving voltage V_R (upper) and tunnel current I_{DC} (lower). Same as Fig. 3b of the main text. All curves in **a,b** except the blue ones are vertically shifted for clarity. ESR conditions in **a**: $V_{DC} = 50$ mV, $I_{DC} = 20$ pA, $V_S = 30$ mV, $\tau_S = 200$ ns. **b**: $V_{DC} = 50$ mV, $V_S = 30$ mV, $V_R = 120$ mV, $\tau_S = 200$ ns.



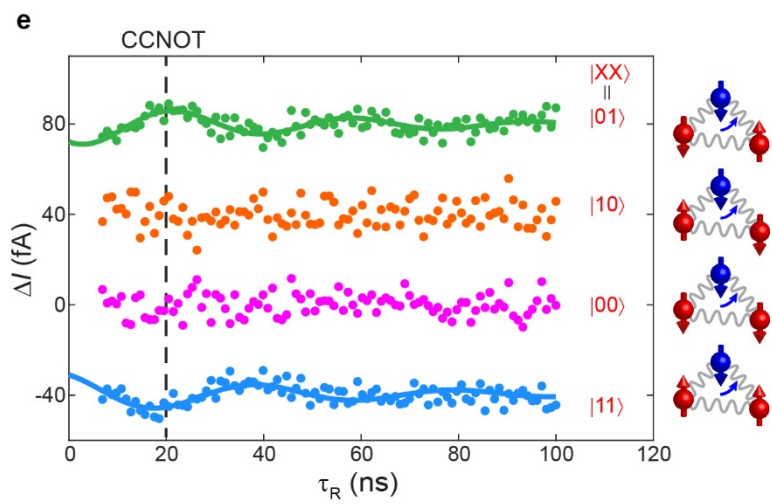
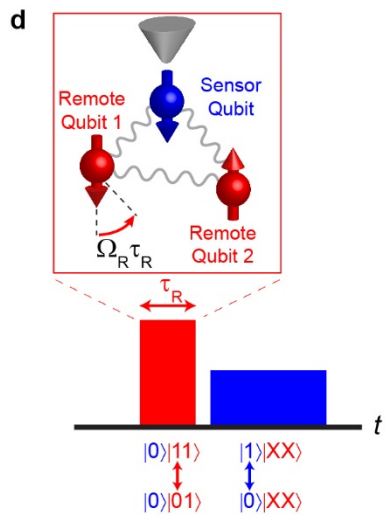
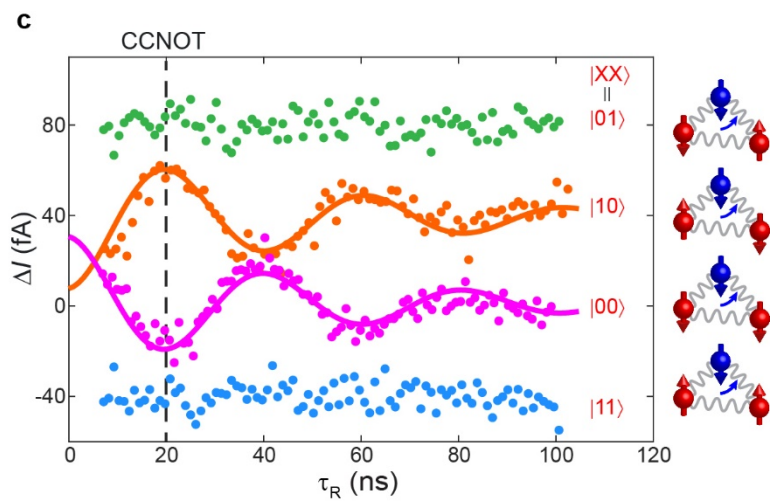
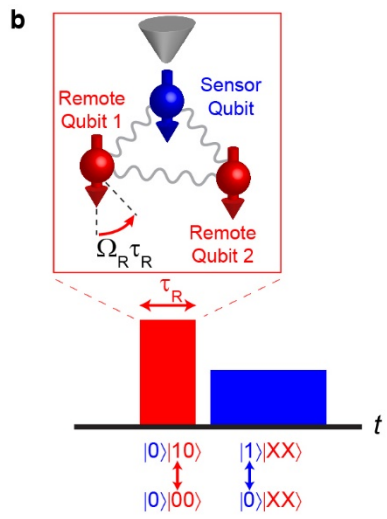
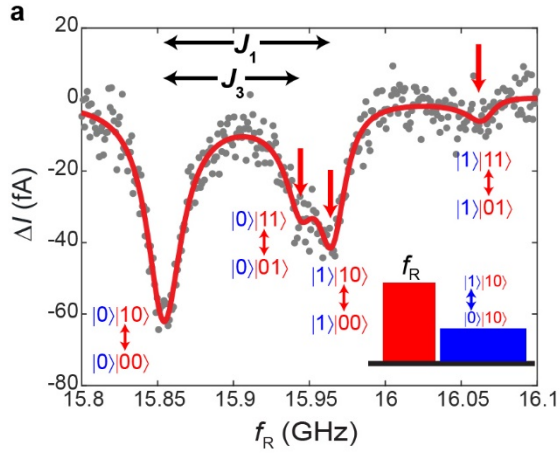
Extended Data Fig. 4 | Controlled rotations of the remote qubit measured with two different sensing frequencies in the two-qubit structure shown in Fig. 1b. Left: Schematics of the pulse sequences and corresponding qubit rotations. Right: Controlled rotations of the remote qubit measured with a sensing pulse applied at f_1 (red) and f_2 (orange). A sensing pulse at f_1 excites the transition $|0\rangle|0\rangle \leftrightarrow |1\rangle|0\rangle$, hence effectively detecting state $|0\rangle$ of the remote qubit³. In contrast, a sensing pulse at f_2 excites the transition $|0\rangle|1\rangle \leftrightarrow |1\rangle|1\rangle$, hence effectively detecting state $|1\rangle$ of the remote qubit. The two oscillations thus show opposite phases. ESR conditions: $V_{DC} = 50$ mV, $I_{DC} = 20$ pA, $V_S = 30$ mV, $V_R = 60$ mV, $\tau_S = 200$ ns.



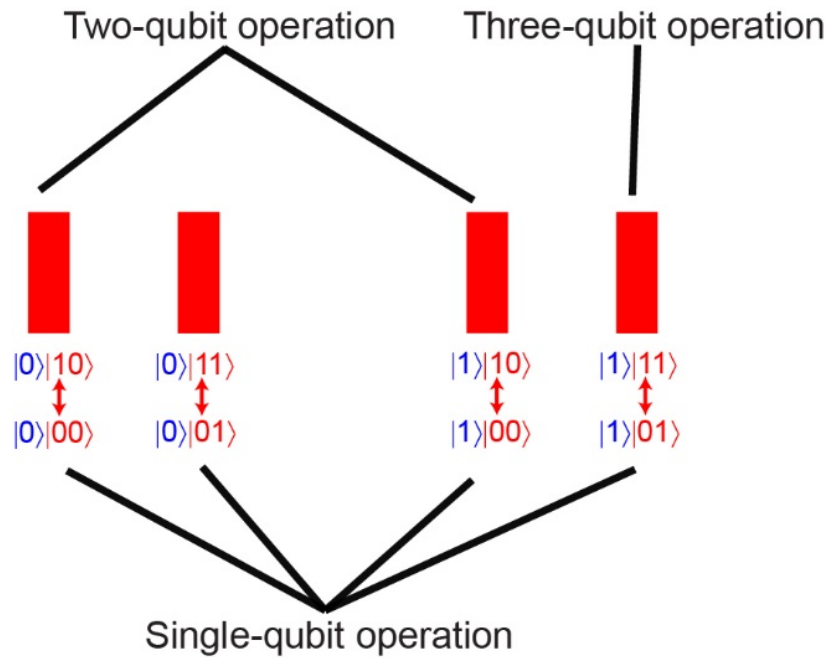
Extended Data Fig. 5 | Controlled oscillations of the remote qubit measured with different magnetic tips in the two-qubit structure shown in Fig. 1b. **a**, Controlled oscillations of a remote qubit measured with different magnetic tips using the same parameters. **b**, Extracted frequencies and amplitudes of the oscillations from data in **a**. Variations of $\Omega/2\pi$ might be related to variations of the tip's effective radius (which affects the radiation range of the RF electric field)⁴ or stability of the tip's magnetic moment (see the main text). Green, orange and magenta curves are vertically shifted for clarity. ESR conditions in **a**: $V_{DC} = 50$ mV, $I_{DC} = 20$ pA, $V_S = 30$ mV, $V_R = 120$ mV, $\tau_S = 200$ ns.



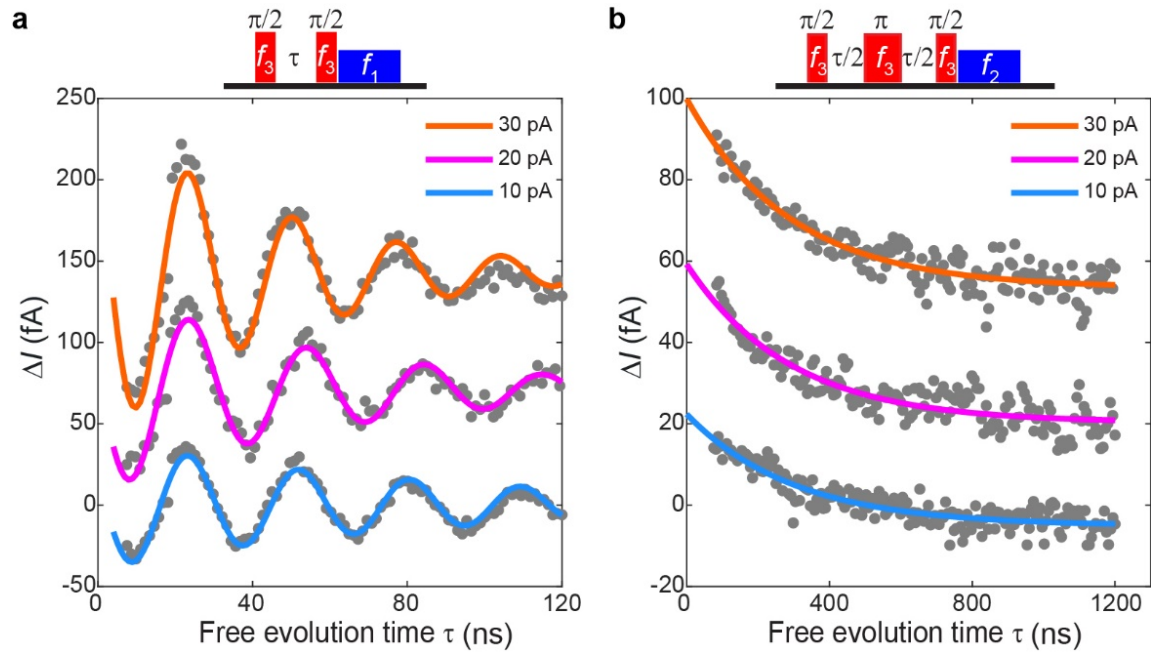
Extended Data Fig. 6 | Controlled rotation of the sensor qubit without and with applying a CNOT operation of the remote qubit, measured in the two-qubit structure shown in Fig. 1b. Blue (cyan) curves measured with $f_S = f_1$ (f_2) correspond to the controlled rotations of the sensor qubit when the remote qubit is in state $|0\rangle$ ($|1\rangle$). **a**, Controlled rotations of the sensor qubit without any operations on the remote qubit. Same as main Fig. 3c. **b**, Controlled rotations of the sensor qubit with a CNOT operation on the remote qubit at $f_R = f_3$, same as main Fig. 3d. **c**, Similar to **b** but with a CNOT operation on the remote qubit at $f_R = f_4$. In **b**, the CNOT operation on the remote qubit at $f_R = f_3$ transfers the predominant thermal population from state $|0\rangle|0\rangle$ to state $|0\rangle|1\rangle$, thus causing the opposite trends of oscillations in **a** and **b**. In contrast, in **c**, the CNOT operation on the remote qubit at $f_R = f_4$ only affects the minor thermal populations in states $|1\rangle|0\rangle$ and $|1\rangle|1\rangle$, thus showing no obvious changes between **c** and **a**. These results highlight the selective, controlled nature of the CNOT operations. Blue curves are shifted vertically by 50 fA for clarity. ESR conditions: **a**: $V_{DC} = 20$ mV, $I_{DC} = 7.5$ pA, $V_S = 100$ mV. **b,c**: $V_{DC} = 20$ mV, $I_{DC} = 7.5$ pA, $V_S = V_R = 100$ mV.



Extended Data Fig. 7 | Controlled-controlled rotations of a remote qubit in the three-qubit structure shown in Fig. 1c. a, ESR spectrum of remote qubit 1 measured with the tip placed on the sensor qubit. The frequency f_R of the remote control pulse is swept while the sensing pulse frequency is fixed at the transition $|0\rangle|10\rangle \leftrightarrow |1\rangle|10\rangle$. This spectrum is used for identifying the frequencies of the remote qubit pulse used in this figure and main Fig. 4. **b,** Schematic showing the control scheme of a CCNOT operation, $|0\rangle|00\rangle \leftrightarrow |0\rangle|10\rangle$, that acts on remote qubit 1. Same as main Fig. 4a. **c,** CCNOT operation of remote qubit 1 by driving the transition $|0\rangle|00\rangle \leftrightarrow |0\rangle|10\rangle$ in the control pulse (red pulse in **c**). Four different frequencies of the sensor qubit are used for readout of the four remote qubit states (red kets). Same as Fig. 4b. **d,e,** Same as **b,c** but with a CCNOT operation at a different transition, $|0\rangle|01\rangle \leftrightarrow |0\rangle|11\rangle$, of remote qubit 1. The CCNOT operation in **b** ($|0\rangle|00\rangle \leftrightarrow |0\rangle|10\rangle$) results in oscillating populations of remote qubits' $|00\rangle$ or $|10\rangle$ states as shown in **c**. The CCNOT operation in **d** ($|0\rangle|01\rangle \leftrightarrow |0\rangle|11\rangle$) results in oscillating populations of remote qubits' $|01\rangle$ or $|11\rangle$ states as shown in **e**. The oscillation amplitude in **e** is smaller due to the smaller thermal populations in remote qubit states $|01\rangle$ and $|11\rangle$. The sinusoidal fits in **c** and **e** show a CCNOT operation time of ~ 20 ns. Green, orange and blue curves are vertically shifted for clarity. ESR conditions in **a**: $V_{DC} = 50$ mV, $I_{DC} = 20$ pA, $V_S = V_R = 30$ mV, $\tau_S = \tau_R = 200$ ns. **c,e**: $V_{DC} = 50$ mV, $I_{DC} = 20$ pA, $V_S = 50$ mV, $V_R = 80$ mV, $\tau_S = 200$ ns.



Extended Data Fig. 8 | Strategy to perform single-, two-, and multi-qubit operations in our platform. Here for simplicity we use a three-qubit structure as an example. Single-qubit operations are performed by non-selectively exciting all ESR transitions of a qubit with the same strength. Two-qubit operations are performed by selectively exciting ESR transitions that correspond to a specific quantum state of one control qubit. Multi-qubit operations are performed by selectively exciting ESR transitions that correspond to a specific quantum state of multiple control qubits.



Extended Data Fig. 9 | Spectra of Ramsey and spin echo measurements corresponding to the data points shown in the insets of Fig. 5b and 5c. Orange and magenta curves are vertically shifted for clarity. The blue curve in **a** is the same as the spectrum shown in main Fig. 5b. The blue curve in **b** is the same as the spectrum shown in main Fig. 5c.

References

- 1 Paul, W., Yang, K., Baumann, S., Romming, N., Choi, T., Lutz, C. P., Heinrich, A. J. Control of the millisecond spin lifetime of an electrically probed atom. *Nature Physics* **13**, 403-407, doi:10.1038/nphys3965 (2016).
- 2 Willke, P., Singha, A., Zhang, X., Esat, T., Lutz, C. P., Heinrich, A. J., Choi, T. Tuning Single-Atom Electron Spin Resonance in a Vector Magnetic Field. *Nano Lett* **19**, 8201-8206, doi:10.1021/acs.nanolett.9b03559 (2019).
- 3 Huang, W., Yang, C. H., Chan, K. W., Tanttu, T., Hensen, B., Leon, R. C. C., Fogarty, M. A., Hwang, J. C. C., Hudson, F. E., Itoh, K. M., Morello, A., Laucht, A., Dzurak, A. S. Fidelity benchmarks for two-qubit gates in silicon. *Nature* **569**, 532-536, doi:10.1038/s41586-019-1197-0 (2019).
- 4 Chu, Z., Zheng, L. & Lai, K. Microwave Microscopy and Its Applications. *Annual Review of Materials Research* **50**, 105-130, doi:10.1146/annurev-matsci-081519-011844 (2020).